3

Prediction of Aerodynamic Characteristics for Elliptic Airfoils in Unmanned Aerial Vehicle Applications

Varun Chitta, Tej P. Dhakal and D. Keith Walters
Mississippi State University,
Starkville, MS,
USA

1. Introduction

Since the mid 1920's, when the first attempt was made to fly a powered pilotless vehicle (Newcome, 2004), significant design improvements for unmanned aerial vehicles (UAV) have been developed, motivated by increased dependence on these vehicles by both civilian and military organizations. Today, the widespread use of UAV's and recent advances in technology resulted in greater interest than ever before for research on these vehicles.

An unmanned vehicle with an additional capability of vertical take-off and landing (VTOL) represents one example of an interest area which has potential for significant research innovation. A canard rotor/wing (CRW) is a UAV that falls under this category. CRWs can hover and fly at low speeds like a conventional helicopter and can also fly at high speeds like a fixed wing aircraft with the additional capability of VTOL (Rutherford et al., 1993; Pandya & Aftosmis, 2001). The CRW has a stoppable two bladed rotor design which allows it to take-off vertically from the ground, transition to a fixed wing aircraft by locking its rotor, and cruise at higher speeds. This specific ability of CRWs to transform into various flight modes makes them an interesting option for military and civilian applications. However, the transition from a rotor blade to a fixed wing vehicle takes place at low speeds, and requires the cross section of rotor blades be elliptic (Kwon & Park, 2005). These considerations motivate research into the aerodynamic characteristics of elliptic airfoils at low/transitional Reynolds numbers (Re).

For lifting surfaces of conventional aircraft, Re is typically well above 10^6 and the turbulent boundary layer does not separate until high angles of attack are encountered (Jahanmiri, 2011). In contrast, UAVs have lower flight velocities and are smaller in size, which results in low wing chord Reynolds numbers ($10^5 < \mathrm{Re} < 2 \times 10^6$) that often lie in the transitional regime. It is well known that, for low Re flows, viscous effects play a much more important role than in high Re flows, in which viscous effects are either neglected or restricted to a thin region near body surface. The complex interactions of viscous mechanisms, transition, and separation present an interesting and challenging problem for UAV design.

For low freestream turbulence intensity (FSTI) and low Re flows, boundary layers are initially laminar and are prone to separation under the influence of even mild adverse

pressure gradients. Once separated, the laminar boundary layer forms a shear layer that may quickly undergo transition to turbulence and reattach to the airfoil surface in the form of a turbulent boundary layer, leading to the formation of a laminar separation bubble (LSB) (Jones, 1938; Diwan & Ramesh, 2007). Shear layer transition occurs due to the amplification of flow instabilities, which cause the shear layer to roll up and form vortices that play a vital role in bubble formation. The enhanced momentum transport in turbulent flow enables flow reattachment and results in development of a turbulent boundary layer on the downstream portion of the airfoil (Sandham, 2008).

The post separation behavior of laminar boundary layers is quite interesting, and accounts for a deterioration of aerodynamic performance of low Re airfoils which is exhibited by an increase in drag and decrease in lift (Yang & Hu, 2008). Experimental results show that airfoil performance starts to deteriorate when chord Re decreases below 5×10^5 (Lissaman, 1983; Carmichael, 1981). Also, if Reynolds numbers are below 5×10^4, the separated shear layer may fail to reattach to the airfoil surface, resulting in a large wake region behind the body (Lin & Pauley, 1996; Yarusevych & Sullivan, 2006) and dramatic loss of performance.

Gaster (Gaster, 1967) was the first to study transition of laminar separation bubbles. As described by Gaster, the separated shear layer formed after laminar boundary layer separation from the suction surface of an airfoil may reattach back to the surface, thereby forming a shallow region of reverse flow known as the separation bubble. A "dead air" region of low velocity is observed under the detached shear layer immediately after separation which results in the formation of a nearly constant region of pressure on the airfoil surface. A strong recirculation zone is observed near the downstream region of bubble. Momentum transfer due to turbulent mixing eliminates the reverse flow due to entrainment of high speed outer fluid, and finally flow reattaches to suction surface (Jahanmiri, 2011).

Depending on the size of bubble, LSB's are typically categorized as either short or long bubbles (Tani, 1964). A long bubble occupies a significant portion of the airfoil surface and affects the inviscid pressure and velocity distributions over much of the airfoil, whereas a short bubble covers only a small portion of airfoil surface and does not affect the pressure and velocity distributions. Figure 1 shows the velocity vector plot of airfoil for SST k-ω model (Menter, 1994) at angle of attack (α) = 7°. For this case, no separation bubble is formed over suction surface of airfoil as the flow is turbulent throughout the surface of airfoil and separation occurs only near the trailing edge. Figure 2 shows a LSB formed on the suction surface near the leading edge of airfoil at α = 7° using the transition-sensitive k-k_L-ω (Walters and Cokljat, 2008) model. The presence of a long separation bubble and post separation behavior of the boundary layer results in increased drag and decreased lift coefficient (Lian & Shyy, 2007).

At high angles of attack, the separated shear layer may fail to reattach to the suction surface and either a long bubble or a completely unattached free shear layer may develop (Gaster, 1967). The change in flow reattachment process due to increasing α depends on the type of airfoil and flow conditions, and might occur gradually or quite sharply. Bubble bursting occurs as a fundamental breakdown of the flow re-attachment process (Horton, 1967). The bursting of the bubble creates an increase in drag, undesirable change in pitching moment and an appreciable drop in lift, causing the airfoil to stall. Figures 3, 4 and 5 show velocity

contours of an elliptic airfoil obtained using the k-k_L-ω model at α = 0º, 7º and 18º respectively. At α = 0º, flow separation is observed on the downstream of portion of the airfoil followed by the formation of two symmetric vortices near the trailing edge. At this angle, the flow is symmetrical over the suction and pressure sides. At α = 7º, a laminar separation bubble is observed on the suction surface near the leading edge of the airfoil. The flow transitions and reattaches as a turbulent boundary layer, and a second flow separation is observed at a location farther downstream on the airfoil surface as compared to the flow separation for the α = 0º case. At α = 18º, bubble bursting takes place and results in a reverse flow over the entire suction surface of airfoil, indicating that the airfoil has stalled.

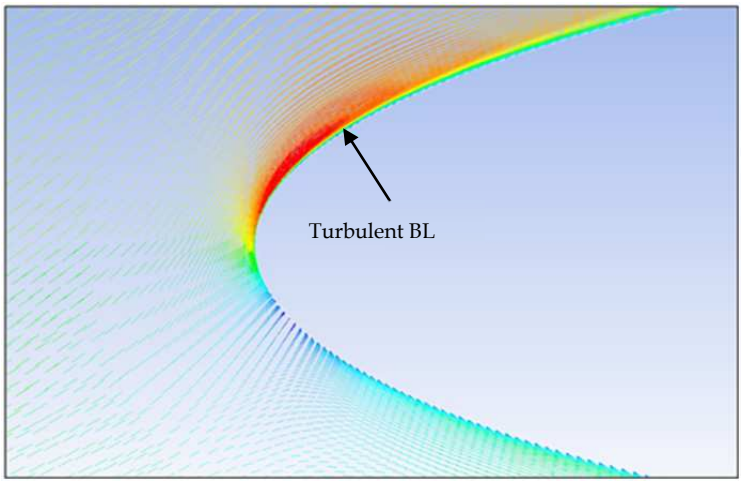

Fig. 1. Velocity vectors near the leading edge of an elliptic airfoil for SST k-ω model at α = 7º. For this case, no separation bubble is observed on the suction surface.

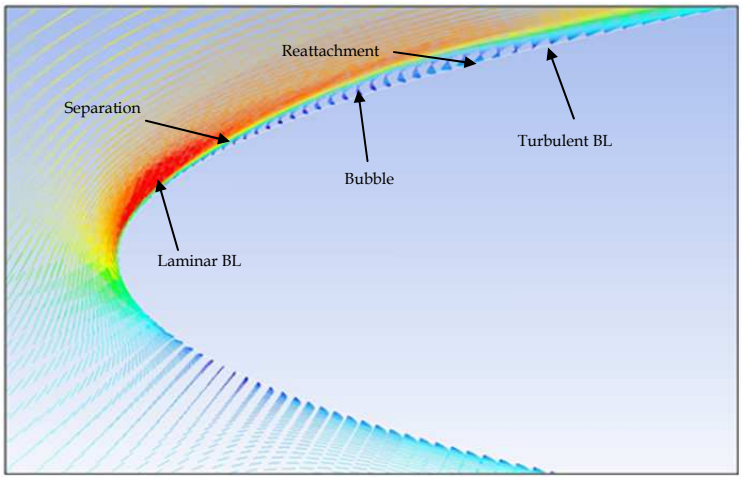

Fig. 2. Laminar separation bubble visible on the suction surface near the leading edge of an elliptic airfoil. Results obtained for k-k_L-ω model at α = 7º.

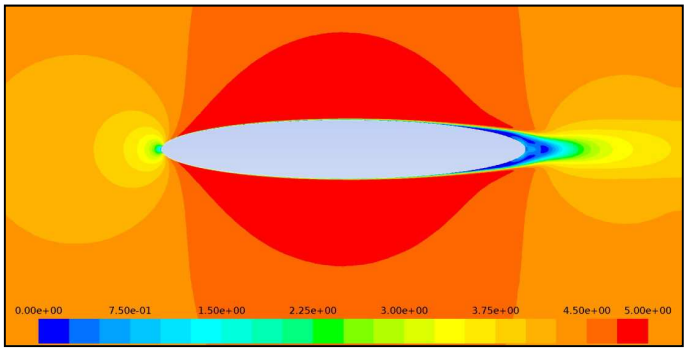

Fig. 3. Velocity contours for k-k_L-ω model at $\alpha = 0^0$. Two opposite and symmetrical vortices are formed near the trailing edge.

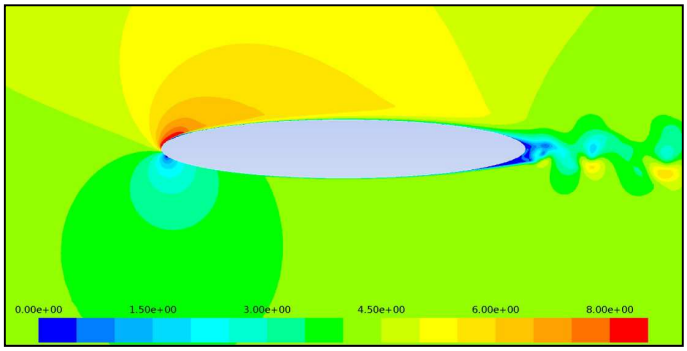

Fig. 4. Velocity contours for k-k_L-ω model at $\alpha = 7^0$. A laminar separation bubble is formed on the suction surface near the leading edge of the airfoil. Vortex shedding is captured by k-k_L-ω for this case and is observed near the trailing edge and in the wake region of airfoil.

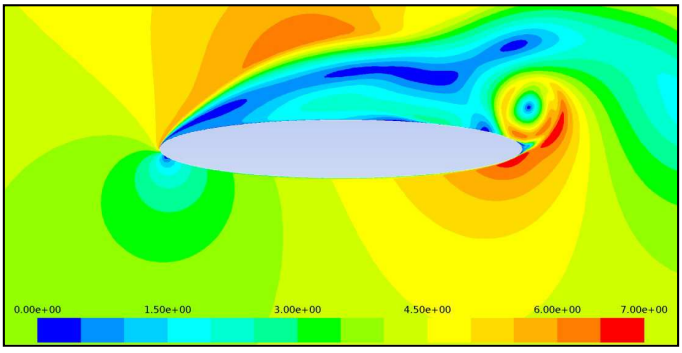

Fig. 5. Velocity contours for k-k_L-ω model at $\alpha = 17^0$. Bubble bursting has occurred and reverse flow over the entire suction surface is observed.

This chapter presents CFD simulations of static elliptic airfoils at varying angles of attack and at relatively low Reynolds numbers ($10^5 < \mathrm{Re} < 2 \times 10^6$), and compares the numerical results with available experimental data (Kwon & Park, 2005). In an effort to facilitate improved understanding of transitional and turbulent flow physics, we have performed numerical simulations using several commercially available fully turbulent and transition-sensitive RANS models, as well as a curvature sensitive fully turbulent RANS model recently developed by our group. Results indicate that a transition-sensitive model is required to accurately reproduce the separation bubble that appears on the suction surface near the leading edge of airfoil over a relatively large range of angles of attack prior to stall. Although the transition-sensitive models—k-k_L-ω (Walters and Cokljat, 2008) and transition-sensitive SST (Menter et al., 2004)—produced reasonable results, both models failed to accurately predict the stall point of airfoil. In contrast, the curvature sensitive SST k-ω-v^2 fully turbulent model (Dhakal and Walters, 2011) predicted the stall point close to experimental results, but it failed to accurately predict the transitional characteristics including flow separation and reattachment in the leading edge region. A comprehensive turbulence model considering both curvature and flow transition effects of airfoil at low Re is not yet available, but our results suggest that such a model would be highly desirable for solving fluid flow problems faced by elliptic airfoils.

The chapter is organized as follows. In the next section we discuss several recent experimental and computational studies related to elliptical bodies in order to provide context for our effort; In section 3 we introduce the computational methodology employed in this work and give the geometric description of the chosen airfoil and the relevant flow parameters. Section 4 presents the numerical results from CFD simulations and provides a discussion on the outcome. In the results section, we also validate the CFD results against available experimental data, and highlight the reasons for discrepancies between experimental and computational results. Section 5 provides a summary and conclusions.

2. Literature review

There are relatively few experimental and computational studies available in the open literature regarding the study of aerodynamic characteristics of elliptic airfoils at transitional Reynolds numbers. This section presents a brief summary of publications most relevant to the current study.

2.1 Experimental studies

Zahm et al. (1929) reported wind tunnel test results for four elliptic cylinders with fineness ratios of 2.5, 3.0, 3.5 and 4.0. Surface pressures and drag characteristics were studied for various yaw angles. Zahm found that, for low Re flows, optimal drag characteristics occurred when the elliptic cylinder had a fineness ratio of 4.0, whereas for high Re flows, improved characteristics were obtained for fineness ratios smaller than 4.0. Schubauer (1939) studied the air flow in the boundary layer on an elliptic cylinder. A conventional hot-wire anemometer was used to measure magnitude and frequency of speed fluctuations in the boundary layer. The study investigated the relationship between boundary layer transition and freestream turbulence intensity for a 33.8% thickness elliptic cylinder at zero angle of attack. Schubauer found that the transition location depended on both the turbulence scale and the freestream turbulence intensity.

Kwon and Park (2005) performed wind tunnel tests for an elliptic airfoil and measured aerodynamic forces and moments for a single airfoil thickness ratio of 16% at Re = 3×10^5. Tests were conducted on an airfoil with and without a boundary layer transition trip with FSTI of 0.12%. Trip devices were attached on both the pressure and suction surfaces of the airfoil at about 10% chord length to induce turbulent flow over the majority of the surface. The boundary layer trip technique is generally used in wind tunnel tests to simulate full scale or high Re flows in low Re airfoil test conditions in a laboratory to enforce transition locations and to eliminate laminar separation bubbles (Kwon et al., 2006). It was found that the lift curve of the elliptic airfoil varied as function of Re and lift did not linearly increase with angle of attack, in contrast to the behavior of conventional airfoils. In the experiment, C_L curves for both smooth and tripped cases behaved similarly when the angle of attack exceeded 6º. Kwon also found that the asymmetric flow separation behavior around the smooth airfoil trailing edge caused a lift curve slope much greater than 2π at low angles of attack which differs from the behavior of conventional airfoils.

Kwon et al. (2006) extended the previous research on elliptic airfoils to study in detail the boundary layer transition process using a particle image velocimetry (PIV) technique. Tests were conducted on the same elliptic airfoil as in Kwon and Park (2005) for the same flow conditions. Velocity profiles were measured and shape factors were calculated from PIV measurements. Intermittency factors were computed from surface mounted hot film sensor measurements. The authors concluded that the unusual aerodynamic characteristics of elliptic airfoils, such as a high lift curve slope and high drag coefficient at low angle of attack, were a consequence of the different flow regimes, i.e. laminar or turbulent, between the suction and pressure surfaces as angle of attack increases.

2.2 Computational studies

Johnson et al. (2001) used a 2D spectral element method to solve the unsteady Navier-Stokes equations to study the vortex structures behind two-dimensional elliptic cylinders. The effects of Re and aspect ratio on Strouhal number, drag coefficient and the onset of vortex shedding were reported for Reynolds numbers from 30 to 200 and aspect ratios ranging from 0.01 to 1. As the aspect ratio of the elliptic cylinder was decreased, the shedding pattern behind the cylinder changed from a periodic Karman vortex street to an aperiodic secondary shedding of vortices. The value of Re at the onset of periodic vortex shedding decreased as aspect ratio decreased. In general, however, this range of Re is too low to be directly applicable in UAV design.

Kim and Sengupta (2005) focused their computational study on the unsteady viscous flow over two dimensional elliptic cylinders by solving the incompressible Navier-Stokes equations for thickness-to-chord ratios of 0.6, 0.8, 1.0 and 1.2, and Re ranging from 200-1000. The total drag force on elliptic cylinders during unsteady viscous airflow mostly comes from the pressure drag force, which increases with an increase of either thickness-to-chord ratio or Re. Also, the mean pressure drag force strongly depends on cylinder thickness, while the mean frictional drag force strongly depends on Re. The frequency of vortex shedding was found to be higher when either the thickness of the elliptic cylinder was reduced or when Re was increased. The authors concluded that both thickness-to-chord ratio and Re have significant effects on vortex shedding and also on the amplitudes of lift and drag forces.

Assel (2007) performed a computational study of flow over elliptic airfoils for a range of Re from 1×10^5 to 8×10^6, by varying the thickness ratios of the airfoils from 5% to 25% and angles of attack from 0 to 20º. He used the Spalart-Allmaras (SA) turbulence model to perform steady-state CFD simulations for the test case. For a Re of 3×10^5 and a thickness ratio of 16%, Assel compared his CFD results with experimentally available wind tunnel test results (Kwon & Park, 2005). Although the stall point of airfoil was reported to be predicted accurately, transitional effects on the airfoil in the CFD simulations did not match with experimental results. The formation of a laminar separation bubble was observed at $\alpha = 8^o$ in the CFD simulations, while Kwon and Park reported the occurrence of transition over the airfoil surface for the smooth case at 6º. Also, CFD results did not possess the unusual aerodynamic characteristics of elliptic airfoils such as high lift curve slope and high drag coefficient at low angle of attack ranges. These discrepancies are likely due in whole or in part to the inability of fully turbulent models to resolve transition effects correctly.

Pandya & Aftosmis (2001) studied the aerodynamic loads on a CRW aircraft using inviscid numerical simulations to understand flight characteristics during conversion from rotary to fixed-wing flight. Although the authors studied the loads acting on different components of the aircraft, little attention was given to the detailed analysis of the fluid mechanics and aerodynamic forces acting on lifting surfaces of aircraft.

To date, CFD simulations of flow over elliptic airfoils have been performed using traditional eddy viscosity models that were developed primarily for high Re applications. Such models are mostly used for predicting fully turbulent flow in which transition effects and rotation and/or curvature effects do not significantly affect the mean flow. Complex flow phenomena like formation of laminar separation bubbles and flow transition from laminar to turbulent are quite commonly encountered in applications of low Re flows. Usage of standard, fully turbulent models for these applications may lead to accuracy degradation in the prediction of flow characteristics as these models do not have the ability to accurately predict the transitional behavior of fluid flow. Recently, the laminar kinetic energy (LKE) concept has led to the recent development of RANS based turbulence models intended to capture the flow transition effects at low Re flows without the use of intermittency factors (Walters, 2009).

An early version of an LKE based model was introduced by Walters & Leylek (2004), which provided a single point RANS approach for transitional flow prediction which eliminates the need for an external linear stability solver or empirical transition correlations. The most recently documented version of the model is the k-k_L-ω model (Walters & Cokljat, 2008). It is a three-equation eddy viscosity model which has transport equations for turbulent kinetic energy (k), laminar kinetic energy (k_L) and specific dissipation rate (ω). As an alternate approach, the Transition SST k-ω model (Menter et al., 2004) has also been introduced as a single-point approach for transitional flow prediction. It is a four-equation model, with two additional transport equations beyond k and ω; one to determine intermittency (γ – equation) and one to determine the transition onset momentum thickness Re ($Re_{\theta t}$ - equation). Recently, Genc et al. (2009, 2011) performed detailed studies to evaluate the performance of the transition-sensitive k-k_L-ω and Transition SST k-ω models versus fully turbulent k-ω SST (Menter, 1994) and k-ε RNG (Choudhury, 1993) models for predicting low Re flows over a NACA 2415 airfoil for a flow Re of 2×10^5. It was shown that both transition-sensitive models improve predictive capability over fully turbulent model form, although differences between the transition-sensitive models were noted.

Most eddy viscosity models also fail to accurately predict the effects of system rotation or streamline curvature, which can enhance or reduce the turbulence intensity in attached boundary layers and separated shear layers. As discussed in the recent review of curvature-sensitized RANS models (Durbin, 2011), convex curvature tends to reduce turbulence intensity while concave curvature tends to enhance it. These effects of curvature are determined by the direction of rotation: along a convex wall, the strain rate tensor rotates in the same direction as the local vorticity vector; along a concave wall, the two rotations are in opposite directions. Co-rotation suppresses turbulence and counter-rotation enhances it. Recently, a new model sensitized to system rotation and streamline curvature was introduced by Dhakal and Walters (Dhakal & Walters, 2011). The model was dubbed SST k-ω-v^2, and includes terms to modify the eddy viscosity in response to local curvature of the mean flowfield.

In this study, both of the transition-sensitive models discussed above—k-k_L-ω and Transition SST k-ω model—are used. Both of these models are incorporated into Ansys FLUENT and are therefore commercially available. These models are used to evaluate the importance of resolving boundary layer transition for analysis of aerodynamic characteristics of low Re elliptic airfoils. Furthermore, results are compared to experimental data in order to validate the capability of the models for accurate prediction of flow physics. Similarly, to evaluate the impact of flow curvature effects on the aerodynamic characteristics of an elliptic airfoil, simulations have also been carried out in this study using the newly developed SST k-ω-v^2 model. Since this model is not currently incorporated into the Ansys FLUENT flow solver, it was implemented using the user-defined function capability available in that solver.

3. Computational methodology

Flow over a two-dimensional elliptic airfoil for a fixed chord Reynolds number of 3×10^5 has been investigated in this study. This Reynolds number was chosen since it lies in the range wherein laminar-to-turbulent boundary layer transition plays a predominant role in determining aerodynamic characteristics. Since both Re and thickness ratio of the airfoil are fixed, a single geometry and mesh for elliptic airfoil was used for all CFD simulations. The surface geometry of the ellipse was defined and the grid was generated using Ansys GAMBIT software.

3.1 Geometry, grid and boundary conditions

The ellipse defining the airfoil surface was oriented in the x-y plane with a unit chord length (c = 1 m) along the positive x-axis and a maximum thickness of 0.16 units in the y-axis located at one half chord length. The upstream, downstream, top, and bottom boundaries were placed at a distance of 10 chord lengths from the ellipse. To ensure that the boundary location did not influence the flow, additional simulations were carried out in which the boundaries were placed at a distance of 20 chord lengths from the ellipse. No significant differences were seen in the results from the different geometries.

To maximize simulation efficiency, a hybrid unstructured grid topology was used. This approach allows the grid to be constructed in such a way that regions of high curvature and large flow gradient can maintain higher point densities. Using these concepts, a structurd O-type grid was generated near the airfoil surface while an unstructured triangular mesh was used for the farfield regions. A total of 480 grid points were placed on airfoil surface in such

a way that more points were clustered in areas of high curvature, near the leading and trailing edges of the airfoil. The density of grid points was stretched vertically from the airfoil surface, and in the unstructured region the mesh size was decreased gradually towards the outer boundaries of the domain. In order to resolve vortex structures in the wake region, a relatively fine grid was maintained downstream of the airfoil.

A mesh boundary layer with a total depth of 0.048 chord units was used. The first point in the viscous layer was placed at a distance of 5e-05 chord units from the wall and thereby increased uniformly upto 48 point layers with a growth factor of 1.1. This spacing corresponded to a y plus value less than unity over the entire airfoil surface. Fig. 6 shows a closeup of the mesh in the vicinity of the airfoil and very near the leading edge. A total of 180,000 cells were used and the same unstructured grid was used for simulation of all turbulence models. A grid resolution study was performed by systematically refining the grid in the region of the airfoil, including both structured and unstructured regions. No considerable changes were seen in the results for meshes larger than 180,000 cells, therefore the baseline mesh was deemed to be grid independent.

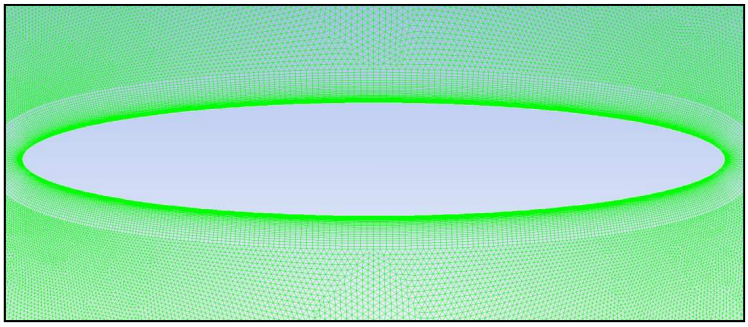

(a)

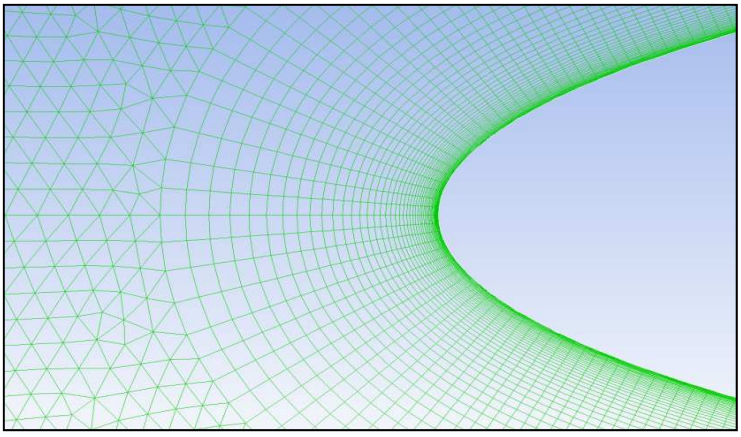

(b)

Fig. 6. Closeup of mesh in the vicinity of the elliptic airfoil (a) and closeup of mesh near the leading edge (b).

The overall domain, grid, and boundary conditions are shown in Fig. 7. The left and bottom sides of the rectangular domain were specified as velocity inlets, the right and top sides as pressure outlets and the elliptic airfoil surface as a wall. Specified inlet boundary conditions included a freestream velocity (U_∞) of 4.3822 m/s, turbulent viscosity ratio of 10 and turbulent intensity of 0.12%. Constant air density of 1.225 kg/m^3 and viscosity of 1.7894×10^{-5} kg/m-s were specified as fluid properties.

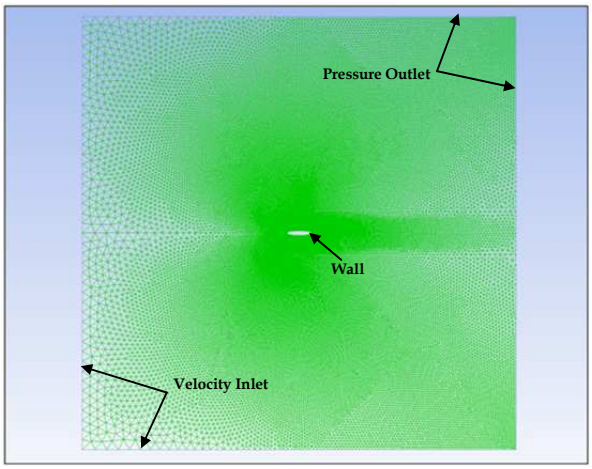

Fig. 7. Computational domain showing overall grid resolution level and boundary conditions.

3.2 Numerical setup

For a steady-state computation, the problem is said to obtain a state of convergence when the solution does not change with additional iterations, while in an unsteady computation, it must be ensured that the solution at each time step is fully converged and time-averaged flow parameters do not change with additional time steps. Simulations with with the Spalart-Allmaras (SA) fully turbulent model obtained steady-state results. For all other fully turbulent and transition-sensitive models, it was necessary to adopt an unsteady RANS (URANS) approach. A fixed time stepping method with a time step size of 0.001T was used for all unsteady simulations with a maximum of 20 iterations per time step, where T is equal to the chord length divided by the freestream velocity (T = c/U_∞). A time-step study was performed, and results obtained with a time step of 0.0005T showed no appreciable change. Unless stated otherwise, all results presented below represent time-averaged quantities.

The simulations used the pressure-based solver in Ansys FLUENT. Convective terms for all equations were discretized using a second-order upwind scheme and unsteady terms were discretized using a second-order implicit scheme for transient simulations. Upwind schemes are generally preferred for spatial discretization in order to obtain accurate results and numerical stability at high Re for incompressible flows (Nair & Sengupta, 1997). The SIMPLE scheme was used for pressure-velocity coupling, and the PRESTO scheme was used for discretization of the pressure terms. Gradients were computed using a Green-Gauss cell based method. Typically, around 6000 time steps were required for the transition-sensitive models and SST k-ω-v^2, and around 4000 time steps were required for the SST k-ω model to

obtain convergence of the time-averaged quantities of flow variables. Around 5000 iterations were required to obtain a converged steady state result for the SA model.

3.3 Turbulence models

One focus of this study is the evaluation of predictive capability of transition-sensitive and curvature-sensitive RANS turbulence models versus traditional eddy-viscosity models for static elliptic airfoils at relatively low Re. Since the flow considered here is in the transitional range, there is a possibility of completely laminar, turbulent or transition from laminar-to-turbulent flow on both suction and pressure surfaces of the airfoil.

The fully turbulent (standard) eddy-viscosity models used for this study include:

- 1-equation SA model (Spalart and Allmaras, 1992)
- 2-equation SST k-ω model (Menter, 1994)

The transition-sensitive eddy-viscosity models used for this study include:

- 3-equation k-k_L-ω model (Walters and Cokljat, 2008)
- 4-equation Transition SST model (Menter et al., 2004)

The curvature-sensitive eddy-viscosity model used for this study is:

- 3-equation SST k-ω-v^2 model (Dhakal and Walters, 2011)

Each of the first four models listed above are available options in Ansys FLUENT. The curvature-sensitive model was implemented into FLUENT by the authors using User-Defined Function (UDF) subroutines.

4. Results

4.1 Airfoil Surface pressure distribution

Fig. 8 shows pressure coefficient profiles for the three fully turbulent models in comparison with experimental results. For $\alpha = 0^o$, all three fully turbulent models; SA, SST k-ω and SST k-ω-v^2, predicted similar results over the suction and pressure surfaces except near the trailing edge, where the SA model predicted a slightly higher pressure than the other two models. This difference is due to the prediction of different flow separation patterns by these models near trailing edge of airfoil. Experimental values for both tripped and smooth cases predicted lower pressure distributions over the surface of airfoil in comparison with fully turbulent models. The experimental data for the tripped case showed higher pressures near the trailing edge in comparison with the smooth case. Not surprisingly, the fully turbulent models showed better agreement with the tripped case in this region, since the tripped boundary layer more closely approximates a boundary layer that is turbulent from the leading edge onward.

As angle of attack was increased, flow velocity increased near the leading edge on the suction surface, causing a sharp decrease of the pressure distribution in that region. Thereafter the pressure gradually increased over the surface as flow approached the trailing edge. Flow velocity also increased over the downstream half of the pressure side causing a decrease of pressure in that region as well. All three of the fully turbulent models predicted similar results over the suction and pressure surfaces of the airfoil. The pressure

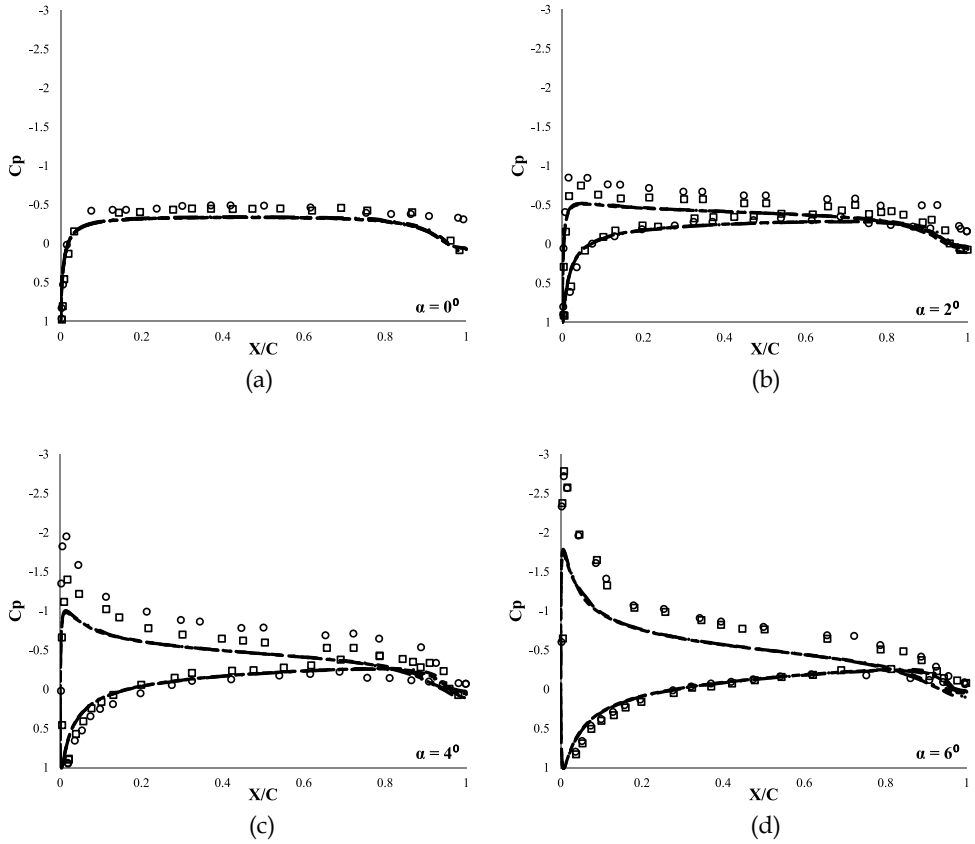

Fig. 8. Pressure coefficient profiles for fully turbulent model cases: ○ Experiment, smooth case (Kwon & Park, 2005); □ Experiment, tripped case; ▪▪▪ SST *k*-ω; ·-·-·-· SA; —·—· SST *k*-ω-v^2.

distribution on the lower surface of the airfoil using the SA, SST *k*-*ω* and SST *k*-*ω*-v^2 models matched well with both smooth and trip case experimental values. Computational results for the suction surface showed overall reasonable agreement with trip case results, but smooth case experimental data show a much lower pressure distribution over the suction surface in comparison with the results of fully turbulent models.

Predicted pressure distributions on the airfoil surface for transition-sensitive models in comparison with experimental and fully turbulent SST *k*-*ω* results are shown in Fig. 9. For α= 0º, the *k*-k_L-*ω* and transition-sensitive SST models predicted similar results over both surfaces except in the region near the trailing edge where flow separates from the suction surface. The transition SST model predicted a higher pressure than the *k*-k_L-*ω* model near trailing edge. Differences in pressure distributions between the SST *k*-*ω* model and both transition-sensitive models for α = 0º can be observed in Fig. 9 (a) on the downstream half of

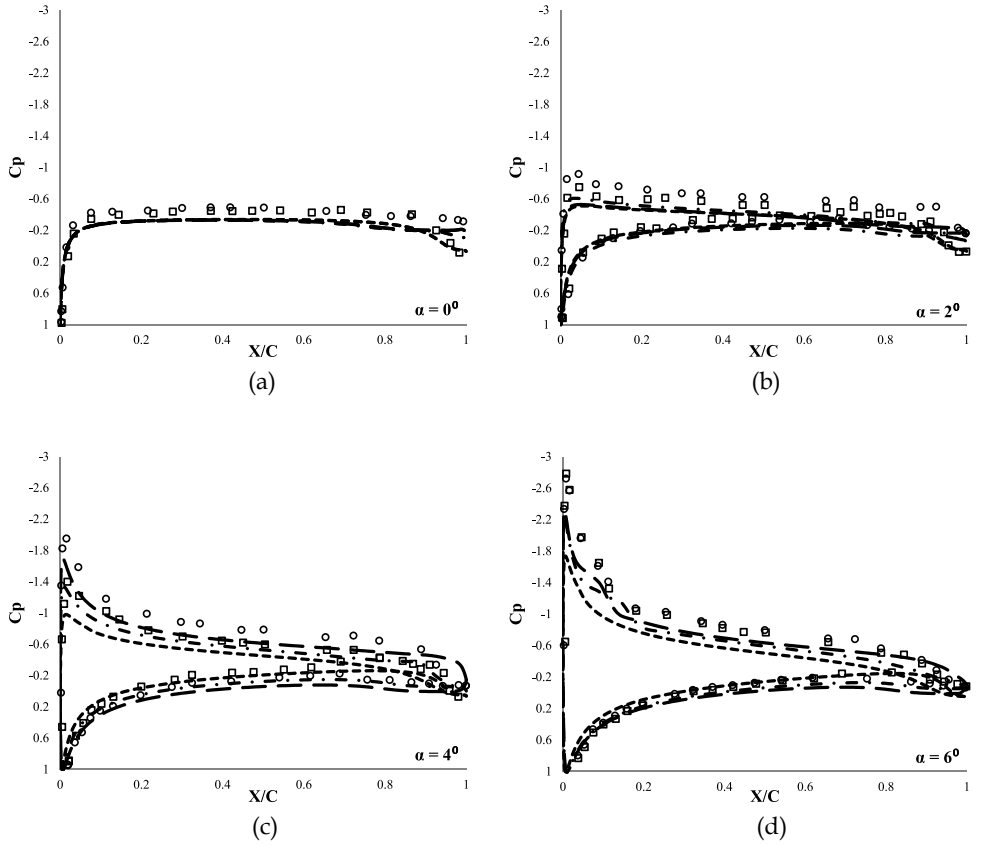

Fig. 9. Pressure coefficient profiles for transition-sensitive model cases: ○ Experiment, smooth case (Kwon & Park, 2005); □ Experiment, tripped case; ▪▪▪▪ SST k-ω; -·-·-·- Transition SST; — — k-k_L-ω.

the surface of airfoil. It appears that the k-k_L-ω model agrees more closely with the smooth case data while the transition SST model agrees with the tripped case data, although the reasons for this are not clear.

For α = 2⁰, interestingly, pressure distributions for the SST k-ω and k-k_L-ω models were similar on the upstream half of the suction surface while further downstream, the SST k-ω model predicted higher pressure than k-k_L-ω. The transition SST model produced the best results for this case, particularly near the leading edge. As α increased, the k-k_L-ω model predicted better results over both the suction and pressure surfaces than the transition SST model, and compared well with the smooth case experimental data. As seen below, the lift coefficients predicted by the k-k_L-ω model were higher than those predicted by the transition SST model and this difference is attributed to the differences in surface pressure

distributions. The k-k_L-ω model predicted significantly lower pressure on the suction surface and higher pressure on the bottom surface when compared to the pressure distributions of the transition SST and SST k-ω models.

While surface pressure distributions on the suction surface varied significantly as angle of attack was increased, similar changes were not observed on the pressure surface. At relatively small α, pressure coefficient profiles on the suction surface were found to rapidly reach their negative peaks near the leading edge and thereafter recover gradually on the downstream portion of the airfoil. At α = 6°, a slight pressure plateau region was found to exist in the experimental data next to a negative pressure peak point, followed by a sudden increase in pressure coefficient next to the plateau region. This characteristic pressure distribution is indicative of formation of a laminar separation bubble near the leading edge (Hu & Yang, 2008). Although a tiny separation bubble was observed in velocity vector plots of SST k-ω, unlike pressure plots of transition-sensitive models, no significant changes were observed in pressure distributions of SST k-ω over suction surface due to presence of separation bubble. This must be due to the size of separation bubble produced in that region. As first explained by Tani (1964) and later reviewed by Shyy et al. (1999) and Lian & Shyy (2007), long separation bubbles generally cover considerable portion of airfoil surface and affect inviscid pressure and velocity distributions around the airfoil, whereas, short bubbles cover small portion of surface and do not affect pressure and velocity distributions.

Both k-k_L-ω and Transition SST models captured the laminar separation bubble formed on suction surface near leading edge of airfoil at α = 6°. The separation bubble stayed on suction surface for a large range of α prior to stall. As α increased, the laminar separation bubble moved towards the leading edge and the size of the bubble reduced gradually. The LSB formed on suction surface can be characterized by a theoretic model given by Russell (Russell, 1979). According to his model, flow separation, transition and reattachment locations on suction surface can be determined by the pressure distribution over the surface of airfoil. The point from where laminar boundary layer separation occurs on airfoil surface refers to separation point. The separated boundary layer undergoes transition to turbulence due to amplification of flow instabilities at transition point and reattaches to airfoil surface as a turbulent boundary layer at reattachment point. The separation bubble formed on a low Re airfoil surface generally includes a laminar and turbulent portion. Distance between separation and transition point is laminar portion and distance between transition and reattachment point is the turbulent portion of bubble (Horton, 1967). At angles of attack greater than 13° for transition SST and 16° for k-k_L-ω, a negative pressure peak near the leading edge was found to decrease and the pressure plateau region became nonexistent. Also, surface pressures on the downstream portion of the airfoil for both suction and pressure sides remained nearly constant. This pressure distribution indicates that the airfoil reached stall at that point.

4.2 Velocity distribution around the airfoil

At α = 0°, the flow over the airfoil was symmetrical and flow separation occurred near the trailing edge. Two attached symmetrical vortices with opposite rotation developed aft of airfoil. As angle of attack was increased, the flow separation point on the suction surface moved towards the leading edge, while the flow separation point on the pressure surface moved towards the trailing edge causing an asymmetric flow around airfoil. The two vortices

aft of the airfoil moved upwards causing the upper vortex to be larger than lower vortex. Figs. 10, 11 and 12 show velocity vector plots for SST k-ω at $\alpha = 0^0$, 7^0 and 12^0 respectively. From Fig. 10, two symmetrical vortices created near the trailing edge of airfoil can be observed. As angle of attack increases, the cross section area of lower vortex gradually decreases and the vortex itself shifts towards the suction side of airfoil. The shift in the locations of vortices near trailing edge can be observed from Figs. 11 and 12. In addition, the leading edge stagnation point moved downwards to pressure side as α increased.

Interestingly, a tiny separation bubble was observed to appear for the fully turbulent SST k-ω and SST k-ω-v^2 models at about $\alpha = 11°$. This bubble stayed near leading edge of the suction surface and finally burst out at $\alpha = 18°$ for SST k-ω and $\alpha = 13°$ for SST k-ω-v^2, causing reverse flow over entire suction surface, indicating that airfoil had stalled. No separation bubbles were observed in simulation results for the SA model.

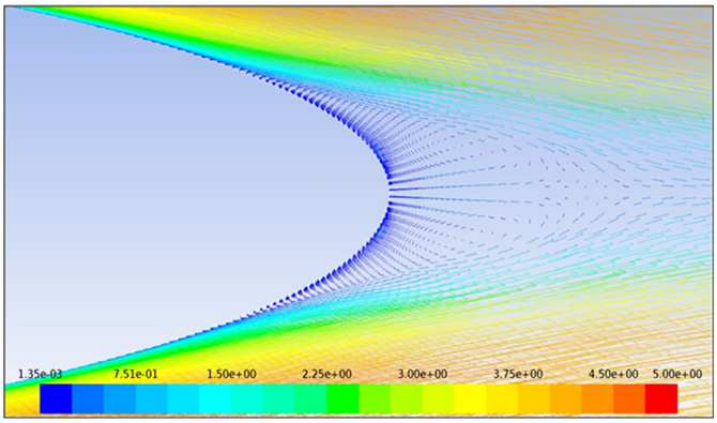

Fig. 10. Velocity vectors near the trailing edge for SST k-ω at $\alpha = 0°$.

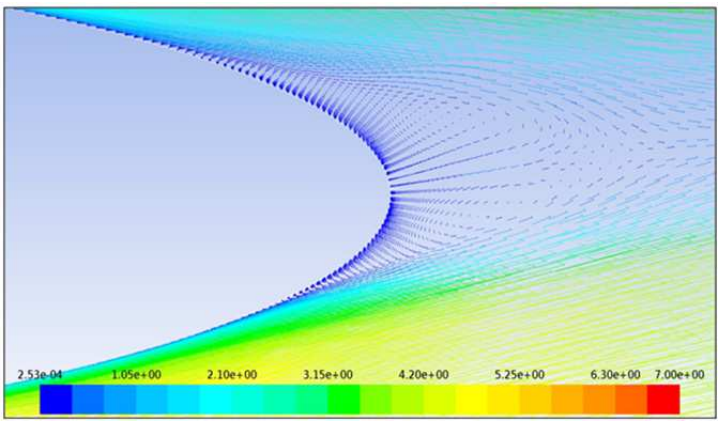

Fig. 11. Velocity vectors near the trailing edge for SST k-ω at $\alpha = 7°$.

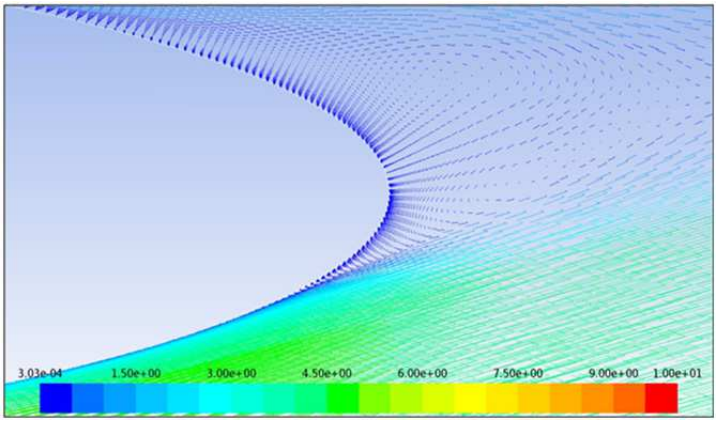

Fig. 12. Velocity vectors near the trailing edge for SST k-ω at $\alpha = 12^{o}$.

For all three fully turbulent models, flow remained attached over most of the airfoil surface and separated at about 95% of chord length at $\alpha = 0^{o}$. As α increased, flow separation points on the suction surface moved towards the leading edge, while flow separation points on pressure surface moved towards the trailing edge. Although for initial angles of attack, flow separated from trailing edge earlier in SST k-ω and SST k-ω-v^2 when compared with SA, a change was observed in flow separation locations for SST k-ω and SST k-ω-v^2 at $\alpha = 11^{o}$. This is likely due to the formation of a tiny separation bubble over leading edge of suction surface mentioned above. The bubble served to keep the flow attached over the surface but as adverse pressure gradient became more severe, the bubble finally burst out resulting in a complete reverse flow over the suction surface.

Flow behavior predicted by the transition-sensitive models was markedly different from that observed for the fully turbulent models. Initially, flow over most of the airfoil surface was laminar for $\alpha = 0^{0}$ to 5^{0} and hence, flow separated earlier from the trailing edge when compared to the flow separation points predicted by the fully turbulent cases. At a flow angle of 6^{0}, the adverse pressure gradient became severe enough that the laminar boundary layer separated, transitioned to turbulent flow and reattached to the suction surface near the leading edge. This flow behavior was captured accurately by both the k-k_L-ω and transition SST models. The reattached turbulent boundary layer was reenergized and hence separated from the suction surface at a farther location significantly farther downstream on the suction surface. As α continued to increase, the separation bubble moved towards the leading edge of the airfoil and the bubble size reduced gradually. As adverse pressure gradient became more severe, the separation bubble burst, resulting in flow reversal over entire suction side of airfoil indicating that the airfoil had stalled.

4.3 Lift and drag coefficients of the airfoil

The lift coefficient (c_l) and drag coefficient (c_d) plots for the fully turbulent model results are shown in Fig. 13 and compared with smooth and tripped case experimental results

(Kwon & Park, 2005). It is observed that all the three fully turbulent models failed to capture the flow transition behavior over the airfoil and hence, a discrepancy in lift coefficient is observed in the CFD results in comparison with experimental results for all values of α prior to stall. Both the SA and SST *k*-*ω* models predicted stall at $\alpha = 17^0$ and 16^0 respectively, which is considerably later than the experimental data indicate. Interestingly, the SST *k*-*ω*-v^2 model predicted a stall point close to experimental results at $\alpha = 12^0$, although lift values prior to stall were still not accurately predicted. However, all three fully turbulent models accurately predicted the drag coefficient values in comparison with experimental results. Discrepancies in c_d values for the SA and SST *k*-*ω* models are only observed at angles of attack greater than 10^0. This is primarily due to the delayed prediction of airfoil stall.

Lift and drag coefficient plots for both transition-sensitive models are shown in Fig. 14 and compared with experimental data and with SST *k*-*ω* results. It was observed previously that the transition sensitive models accurately predict the flow transition behavior, yielding laminar boundary layers up to 6^0 and separation bubbles near the leading edge for $\alpha > 6^0$. As a consequence, the slope of the lift coefficient for $\alpha < 6^0$ was greater than for the fully turbulent models and in better agreement with the experimental data. The formation of the laminar separation bubble caused a shift in the lift curve slope between $\alpha = 4^0$ and 6^0, and the lift curve slope approximately matched the fully turbulent models beyond that point. Although flow transition behavior was captured accurately by both *k*-k_L-*ω* and transition SST models, they notably failed to predict the airfoil stall point, although the transition SST model yields a closer result than the *k*-k_L-*ω* model. The c_d values of both transition-sensitive models compared relatively well with experimental results prior to the stall point. Observing Figs. 13 and 14, the results of this study seem to suggest that accurate prediction of aerodynamic characteristics using linear eddy-viscosity RANS models can be best achieved by a combination of transition-sensitive modeling, which is necessary to predict increased lift values prior to stall, and curvature-sensitive modeling, which is necessary to correctly resolve the stall point.

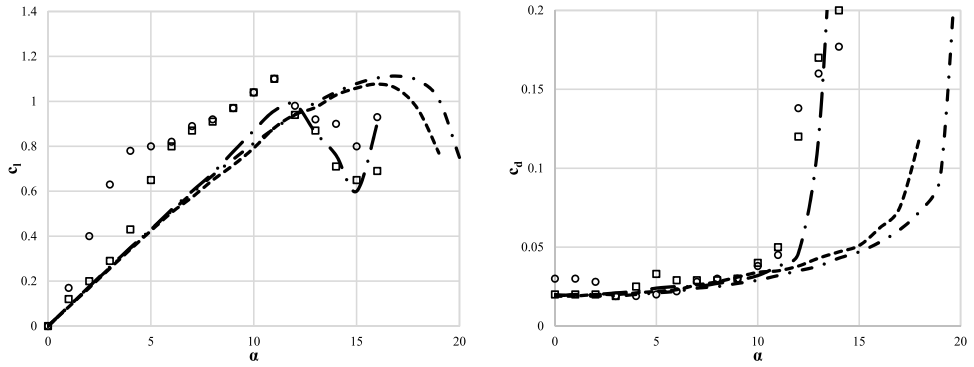

Fig. 13. Lift and drag coefficient curves for fully turbulent models: ○ Experiment, smooth case (Kwon & Park, 2005); □ Experiment, tripped case; ▪▪▪ SST *k*-ω; -·-·-· SA; —·— SST *k*-ω-v^2.

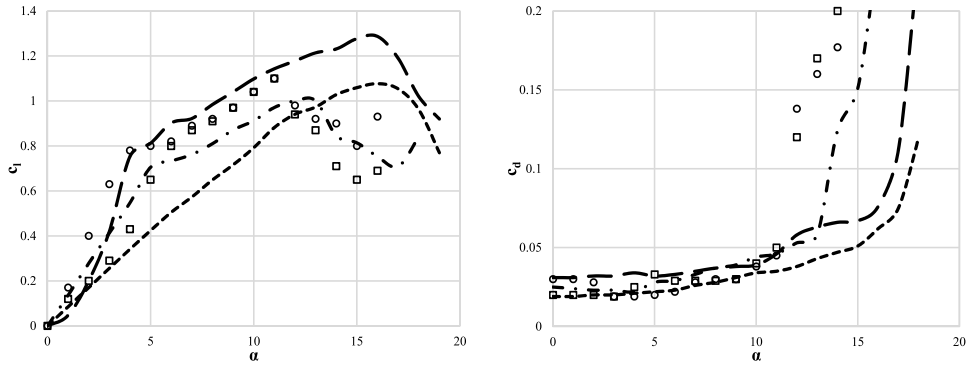

Fig. 14. Lift and drag coefficient curves for transition-sensitive models: ○ Experiment, smooth case (Kwon & Park, 2005); □ Experiment, tripped case; ▪▪▪▪ SST k-ω; -·-·-·- Transition SST; — — k-k_L-ω.

5. Conclusions

Numerical simulations were performed for flow over an elliptic airfoil at varying angles of attack and at a low/transitional Reynolds number of 3×10^5. Simulations were carried out using relatively new transition- and curvature-sensitive eddy viscosity RANS models as well as traditional fully turbulent eddy viscosity models. CFD results were compared to the wind tunnel experimental test results of Kwon & Park (2005). Results indicate that the transition-sensitive models are indeed necessary to accurately predict the transition and separation flow behavior on the suction surface of the airfoil. Both transition-sensitive models—k-k_L-ω and transition SST—reproduce the separation bubble that appears near the leading edge of the airfoil over a relatively large range of angle of attack prior to stall. Consequently, the lift characteristics were better predicted, showing elevated levels and nonlinear increase similar to the experimental data. In contrast, the fully turbulent models—SA, SST k-ω and curvature-sensitive SST k-ω-v^2—failed to accurately predict the boundary layer separation and reattachment phenomena and therefore showed large discrepancies in lift prediction. Although the SST k-ω and SST k-ω-v^2 models predicted a small separation bubble near the leading edge at $\alpha = 11°$, the effect of the separation bubble on pressure and velocity distributions over the airfoil surface was minimal. Interestingly, both the transition-sensitive models as well as the SA and SST k-ω fully turbulent models failed to accurately predict the stall point. However, the curvature sensitive SST k-ω-v^2 successfully predicted the stall point very close to experimental results. These results indicate that accurate RANS prediction of aerodynamic characteristics both pre- and post-stall require models that respond correctly to transitional as well as curvature effects. While a comprehensive turbulence model considering both curvature and flow transition effects at low Reynolds numbers is not yet available, future research efforts will seek to integrate the existing models used here to improve overall predictive capability for these problems.

6. References

Assel, T. W. (2007). Computational study of flow over elliptic airfoils for rotor/wing unmanned aerial vehicle applications, Thesis/Dissertation, University of Missouri – Rolla

Carmichael, B.H. (1981). Low Reynolds Number Airfoil Survey. NASA CR – 165803, Vol. 1

Choudhury, D. (1993). Introduction to the renormalization group method and turbulence modeling, Fluent Inc. Technical Memorandum, TM-107

Dhakal, T. P. & Walters, D. K. (2011). A Three-Equation Variant of the SST k-ω Model Sensitized to Rotation and Curvature Effects. *J Fluid Eng - T ASME,* Vol. 133, No. 11, (November 2011), pp. 11201:1-9

Diwan, S. S. & Ramesh, O. N. (2007). Laminar separation bubbles: Dynamics and Control. *Sadhana*, Vol. 32, Parts 1 & 2, (April 2007), pp. 103-109

Durbin, P. (2011). Review: Adapting Scalar Turbulence Closure Models for Rotation and Curvature. *J Fluid Eng - T ASME*, Vol. 133, (June 2011), pp. 061205:1-8

Gaster, M. (1967). The Structure and Behavior of Separation Bubbles. Reports and Memoranda No. 3595. pp. 1-9

Genc, M. S.; Kaynak, U. & Lock, G. D. (2009). Flow over an aerofoil without and with a leading-edge slat at a transitional Reynolds number, *Proceedings of the Institutions of Mechanical Engineers, Part G: Journal of Aerospace Engineering,* (March 2009), Vol. 223, pp. 217-231

Genc, M. S.; Kaynak, U. & Yapici, H. (2011). Performance of Transition Model for Predicting Low Re Aerofoil Flows without/with Single and Simultaneous Blowing and Suction. *European Journal of Mechanics B/Fluids,* pp. 218-235

Horton, H. P. (1967). A Semi-empirical Theory for the Growth and Bursting of Laminar Separation Bubbles. PhD thesis, Queen Mary College, University of London

Hu, H. & Yang, Z. (2008). An Experimental Study of the Laminar Flow Separation on a Low-Reynolds–Number Airfoil. *J Fluid Eng - T ASME,* Vol. 130, (May 2008), pp. 1-11

Jahanmiri, M. (2011). Laminar Separation Bubble: Its Structure, Dynamics and Control. Research Report, ISSN 1652-8549

Johnson, S. A., Thompson, M. C. & Hourigan, K. (2001). Flow Past Elliptical Cylinders at Low Reynolds Numbers, *Proceedings of AFMS 2001 14th Australasian Fluid Mechanics Conference*, Adelaide University, Adelaide, Australia, December 10-14, 2001

Jones, B. M. (1938). Stalling. *Journal of the Royal Aeronautical Society*, Vol. 38, pp. 747-770

Kim, M. S. & Sengupta, A. (2005). Unsteady Viscous Flow over Elliptic Cylinders At Various Thickness with Different Reynolds Numbers. *Journal of Mechanical Science and Technology,* Vol. 19, No. 3, (December 2005), pp. 877-886

Kwon, K. & Park, S. O. (2005). Aerodynamic Characteristics of an Elliptic Airfoil at Low Reynolds Number. *Journal of Aircraft*, Vol. 42, No. 6, (December 2005), pp. 1642-1644

Kwon, K.; Chang, B.; Lee, J. & Park, S. O. (2006). Boundary Layer Transition Measurement over an Airfoil by Using PIV with High Magnification. Lisbon, Portugal, pp. 1-8

Lian, Y. & Shyy, W. (2007). Laminar-Turbulent Transition of a Low Reynolds Number Rigid or Flexible Airfoil. *AIAA Journal*, Vol. 45, No. 7, (July 2007), pp. 1501-1513, ISSN 0001-1452

Lin, J. C. M. & Pauley, L. L. (1996). Low-Reynolds number separation on an airfoil. *AIAA Journal*, Vol. 34, No. 8, pp. 1570-1577.

Lissaman, P. B. S. (1983). Low Reynolds Number Airfoils. *Annual Review Fluid Mechanics*, No. 15, pp. 223-239

Menter, F. (1994). Two-equation eddy viscosity turbulence models for engineering applications. *AIAA Journal*, Vol. 32, No. 8, pp. 1598-1605, ISSN 0001-1452

Menter, F. R.; Langtry, S. R.; Likki, Y. B.; Suzen, P. G.; Huang, S. & Volker. (2004) A Correlation Based Transition Model Using Local Variables. *Proceedings of ASME Turbo Expo 2004,* ISBN GT2004-53452, Vienna, Austria, pp. 57-67

Nair, M. T. & Sengupta, T. K. (1997). Unsteady Flow Past Elliptical Cylinders. *Journal of Fluids and Structures*, Vol. 11, No. 6, (August 1997), pp. 555-595

Newcome, L. R. (2004). *Unmanned Aviation: A Brief History of Unmanned Aerial Vehicles*, American Institute of Aeronautics and Astronautics (AIAA), ISBN 1-56347-644-4, Virginia, USA

Pandya, S. A. & Aftosmis, M. J. (2001). Computation of External Aerodynamics for a Canard Rotor/Wing Aircraft, *Proceedings of AIAA 2001 39th AIAA Aerospace Sciences Meeting and Exhibit,* Reno, Nevada, USA, January 8-11, 2001

Russell, J. (1979). Length and Bursting of Separation Bubbles: A Physical Interpretation, *Proceedings of Science and Technology of Low Speed Motorless Flight NASA Conference*

Rutherford, J. W.; Bass, S.M. & Larsen, S. D. (1993). Canard Rotor/Wing: A Revolutionary High-Speed Rotorcraft Concept. *AIAA paper 93-1175*, (February 1993)

Sandham, N. D. (2008). Transitional Separation Bubbles and Unsteady Aspects of Aerofoil Stall. *The Aeronautical Journal,* Vol. 112, No. 1133, (July 2008), pp. 395-404

Schubauer, G. B. Air Flow in Boundary Layer of an Elliptic Cylinder. *National Advisory Committee for Aeronautics*, Report No. 652, pp. 207-226

Shyy, W.; Berg, M. & Ljungqvist, D. (1999). Flapping and Flexible Wings for Biological and Micro Vehicles. *Progress in Aerospace Sciences*, Vol. 35, No. 5, pp. 455-506

Spalart, P. R. & Allmaras, S. R. (1992) A One-Equation Turbulence Model for Aerodynamic Flows. AIAA Paper No. 92-0439.

Tani, I. (1964). Low Speed Flows Involving Bubble Separation. *Progress in Aerospace Sciences*, Vol. 5, pp. 70-103

Walters, D. K. & Cokljat, D. (2008). A Three-Equation Eddy-Viscosity Model for Reynolds-Averaged Navier-Stokes Simulations of Transitional Flow. *J Fluid Eng - T ASME*, Vol. 130, (December 2008), pp. 121401:1-14

Walters, D. K. & Leylek, J. H. (2004) A New Model for Boundary Layer Transition Using a Single-Point RANS Approach. *Journal of Turbomachinery*, Vol. 126, No. 1, (January 2004), pp. 193-202, ISSN 0889-504X

Walters, D. K. Physical Interpretation of Transition-Sensitive RANS Models Employing the Laminar Kinetic Energy Concept. *ERCOFTAC Bulletin*, Vol. 80, pp. 67-71.

Yang, Z. & Hu, H. (2008). Laminar Flow Separation and Transition on a Low-Reynolds-Number Airfoil. *Journal of Aircraft,* Vol. 45, No. 3, (June 2008), pp. 1067-1070

Yarusevych, S.; Sullivan, P. E. & Kawall, J. G. (2006). Coherent Structures in an Airfoil Boundary Layer and Wake at Low Reynolds Numbers. *American Institute of Physics*, (April 2006), Vol. 18, pp. 1-11

Zahm, A.F.; Smith, R.H. & Louden, F. A. Forces on Elliptic Cylinders in Uniform Air Stream. *National Advisory Committee for Aeronautics*, Report No. 289, pp. 215-232

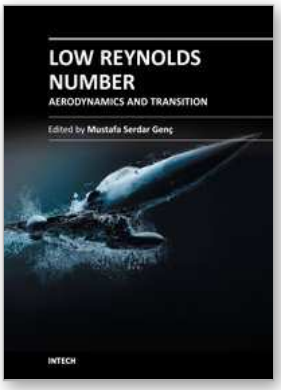

Low Reynolds Number Aerodynamics and Transition

Edited by Dr. Mustafa Serdar Genc

ISBN 978-953-51-0492-6
Hard cover, 162 pages
Publisher InTech
Published online 04, April, 2012
Published in print edition April, 2012

This book reports the latest development and trends in the low Re number aerodynamics, transition from laminar to turbulence, unsteady low Reynolds number flows, experimental studies, numerical transition modelling, control of low Re number flows, and MAV wing aerodynamics. The contributors to each chapter are fluid mechanics and aerodynamics scientists and engineers with strong expertise in their respective fields. As a whole, the studies presented here reveal important new directions toward the realization of applications of MAV and wind turbine blades.

InTech Europe
University Campus STeP Ri
Slavka Krautzeka 83/A
51000 Rijeka, Croatia
Phone: +385 (51) 770 447
Fax: +385 (51) 686 166
www.intechopen.com

InTech China
Unit 405, Office Block, Hotel Equatorial Shanghai
No.65, Yan An Road (West), Shanghai, 200040, China
中国上海市延安西路65号上海国际贵都大饭店办公楼405单元
Phone: +86-21-62489820
Fax: +86-21-62489821